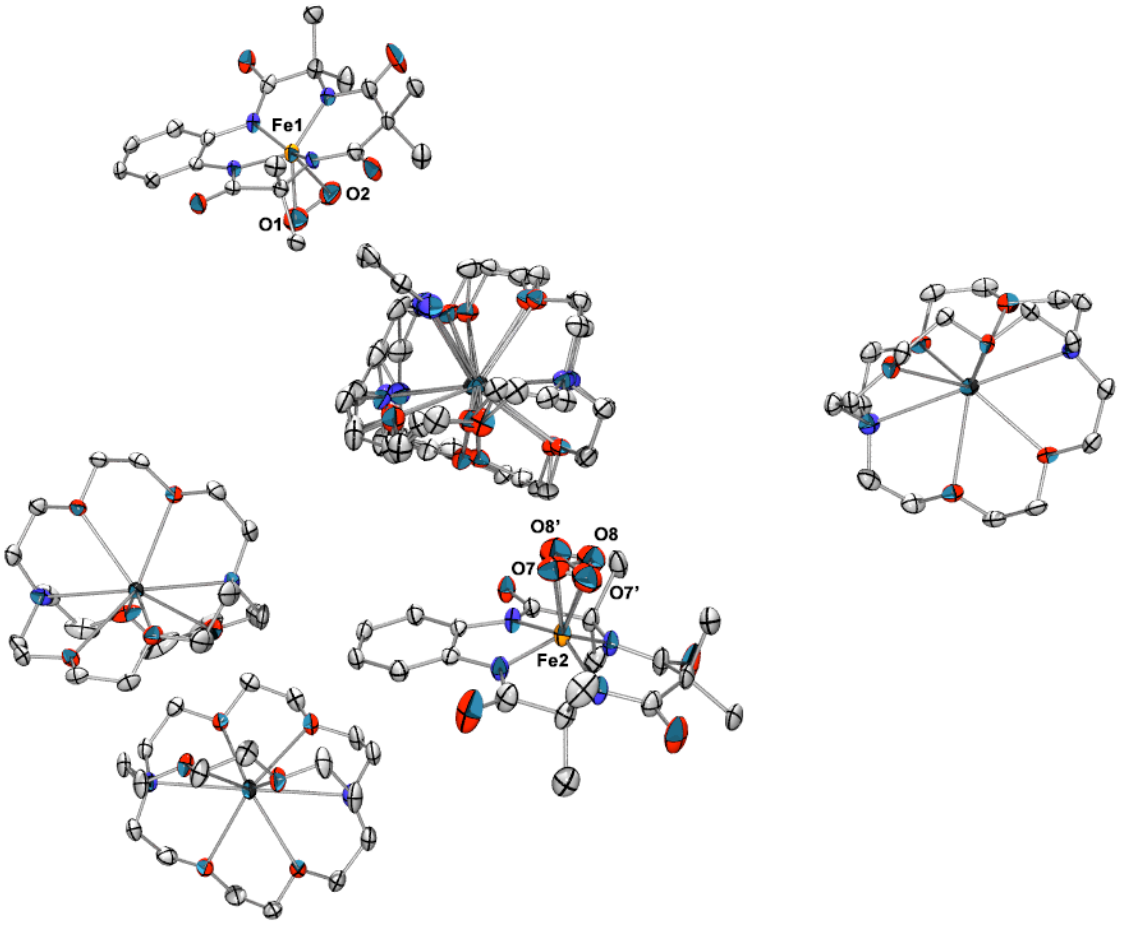

Supplementary Figure 1. Molecular structure of [K(2.2.2-cryptand)(CH_3CN)][K(2.2.2-cryptand)]$_3$-[Fe^{III}(TAML)(O_2)]$_2$ with 30% probability displacement ellipsoids. Hydrogen atoms were omitted for clarity. One of the [Fe^{III}(TAML)(O_2)]$^{2-}$ moieties has the positional disorder of the superoxo group. One of the cation complexes, [K(2.2.2-cryptand)(CH_3CN)]$^+$, also has the positional disorders.

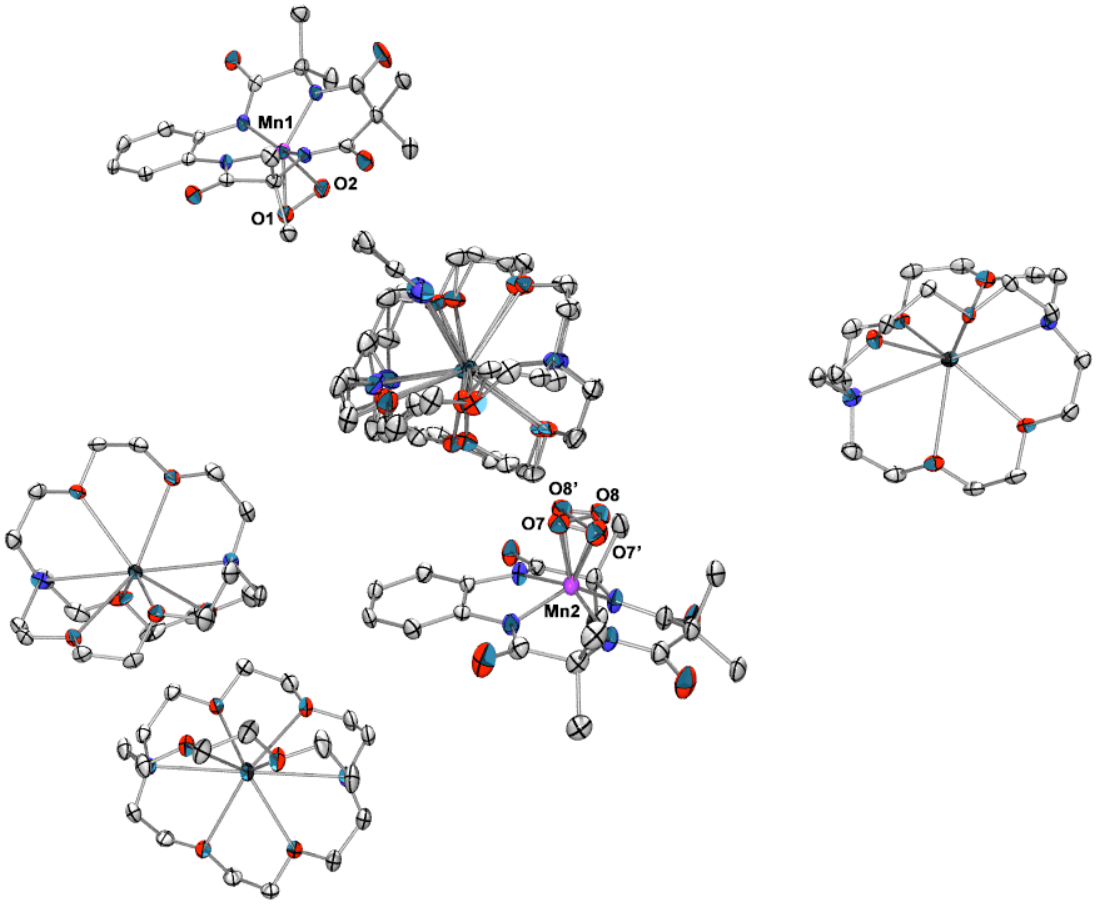

Supplementary Figure 2. Molecular structure of [K(2.2.2-cryptand)(CH_3CN)][K(2.2.2-cryptand)]$_3$ [Mn^{IV}(TAML)(O_2)]$_2$ with 30% probability displacement ellipsoids. Hydrogen atoms were omitted for clarity. One of the [Mn^{IV}(TAML)(O_2)]$^{2-}$ moieties has the positional disorder of the peroxo ligand. One of the cation complexes, [K(2.2.2-cryptand)(CH_3CN)]$^+$, also has the positional disorders.

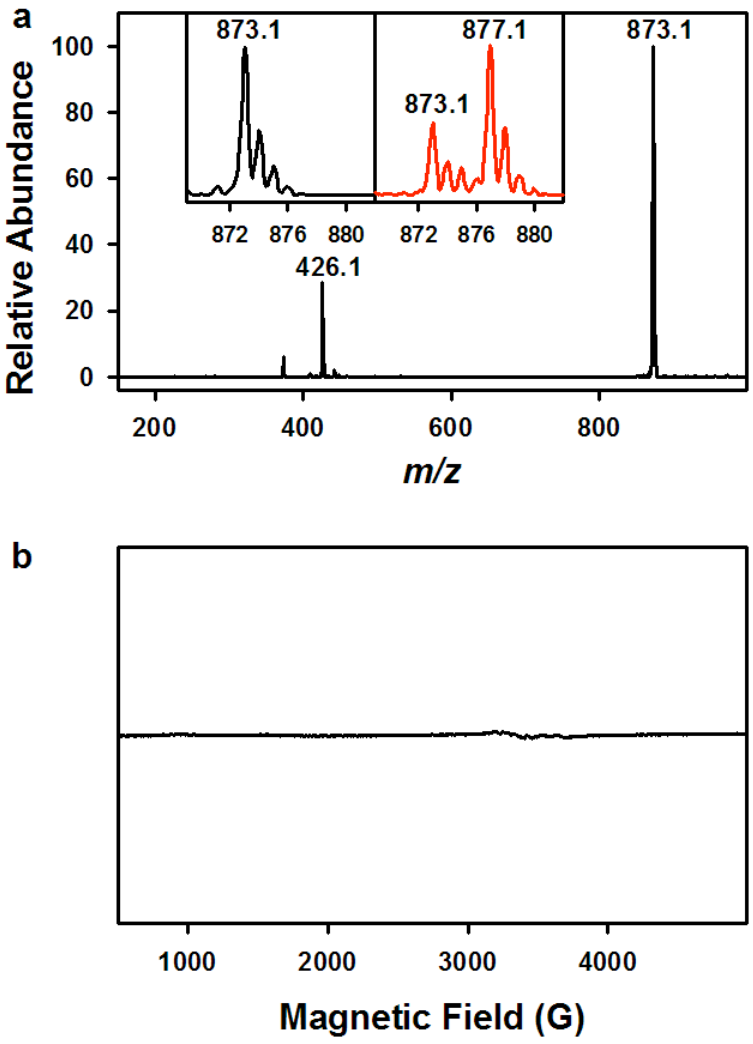

Supplementary Figure 3. a, A full range of negative mode ESI MS spectrum of **1** (0.25 mM) in CH_3CN at –20 °C. Insets show isotope distribution patterns of [K(2.2.2-cryptand)Fe(TAML)($^{16}O_2$)]$^-$ (**1-$^{16}O_2$**) (left panel, black line) and [K(2.2.2-cryptand)Fe(TAML)($^{18}O_2$)]$^-$ (**1-$^{18}O_2$**) (right panel, red line). The peak at *m/z* 426.1 corresponds to [Fe(TAML)]$^-$. **b**, X-band EPR spectrum of **1** (1.0 mM) in CH_3CN at 4.3 K. Spectral conditions: microwave power = 1.0 mW, frequency = 9.647 GHz, receive gain = 1.0×10^4, modulation amplitude = 10 G, and modulation frequency = 100 kHz.

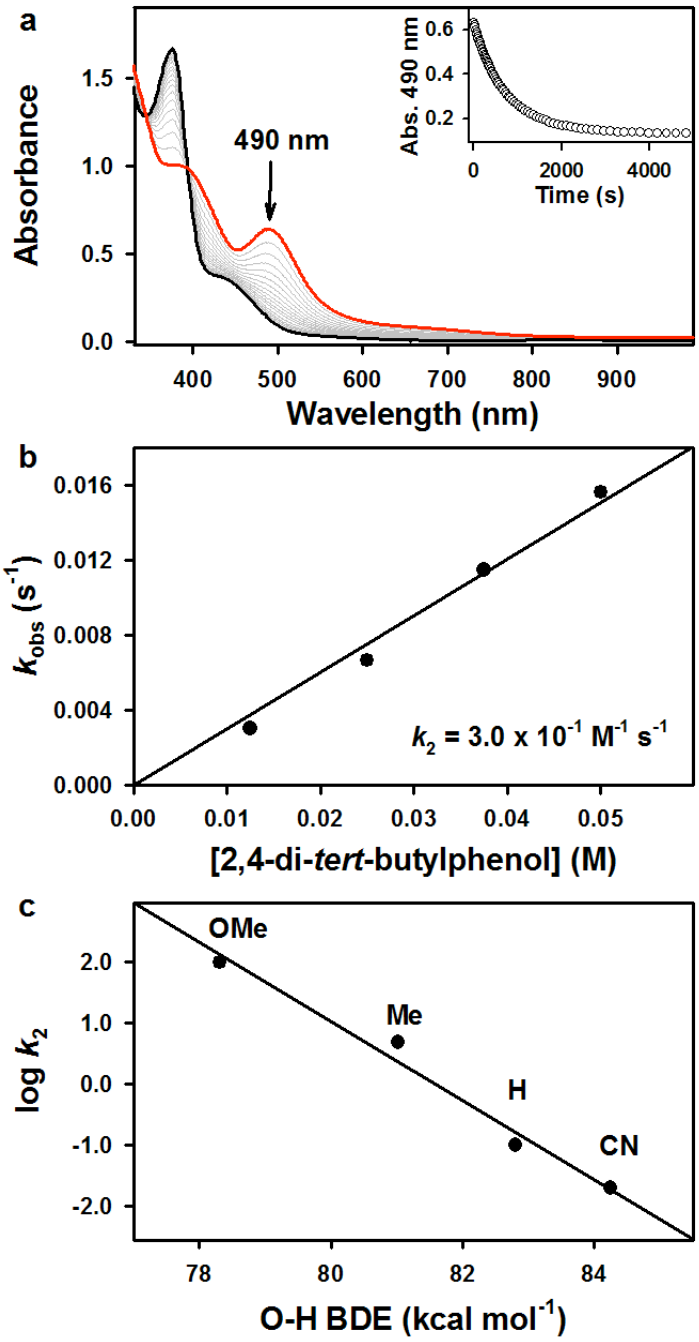

Supplementary Figure 4. **a**, UV-vis spectral changes showing the decay of **1** (0.25 mM) upon addition of 2,4-di-*tert*-butylphenol (5.0 mM) in CH_3CN at –20 °C. Inset shows the time course of the absorbance change of **1** at 490 nm. **b**, Second-order rate constant determined in the reaction of **1** with 2,4-di-*tert*-butylphenol. **c**, Plot of log k_2 of **1** against O-H bond dissociation energies (BDEs) of *para*-Y-2,6-di-*tert*-butylphenols (*p*-Y-2,6-*t*-Bu_2-C_6H_2OH) [Y = OMe, Me, H, CN] in CH_3CN at –20 °C.

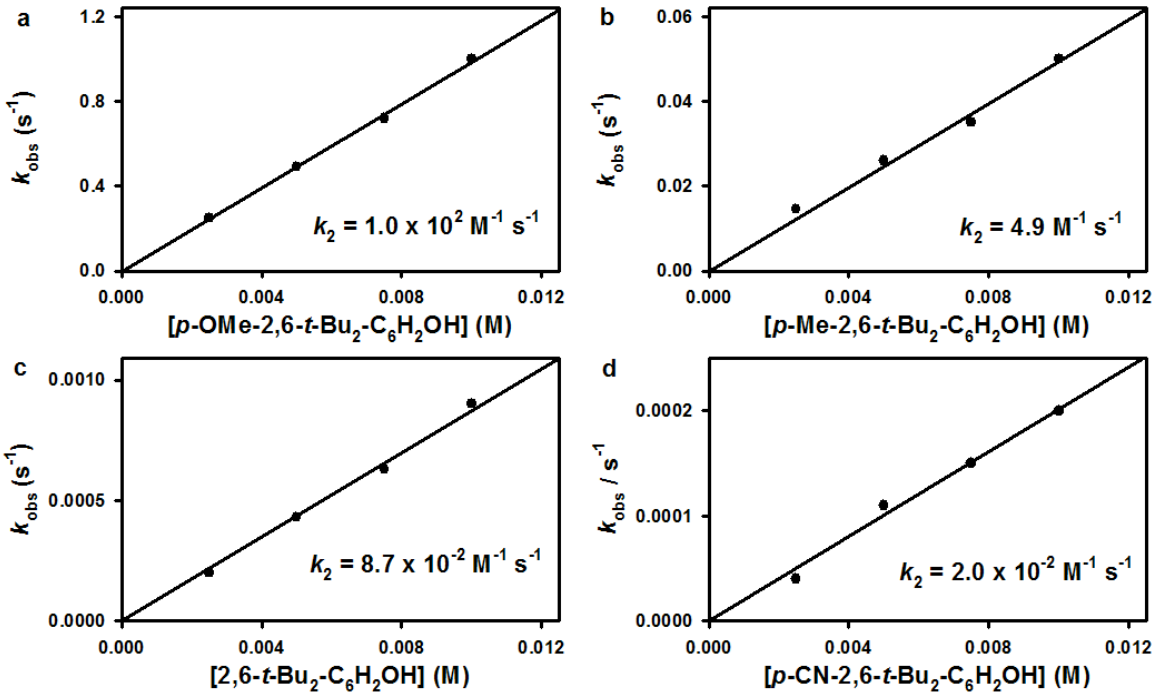

Supplementary Figure 5. Plot of pseudo-first-order rate constants (k_{obs}) against the concentration of *p*-Y-2,6-*t*-Bu_2-C_6H_2OH [Y = OMe (**a**), Me (**b**), H (**c**), CN (**d**)] in the O-H bond activation reaction by **1** in CH_3CN at –20 ^oC.

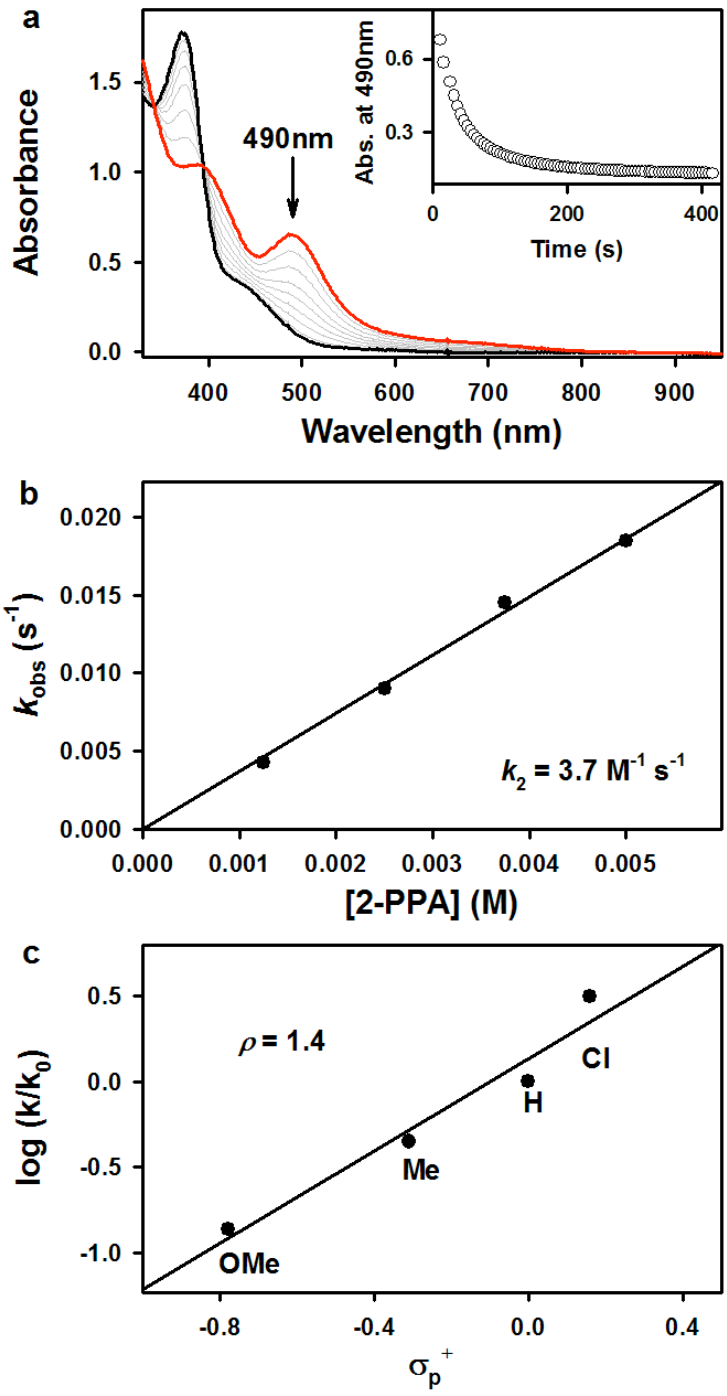

Supplementary Figure 6. **a**, UV-vis spectral changes showing the decay of **1** (0.25 mM) upon addition of 2-phenylpropionaldehyde (2-PPA, 5.0 mM) in CH_3CN at 5 ^oC. Inset shows the time course of the absorbance change of **1** at 490 nm. **b**, Second-order rate constant determined in the reaction of **1** with 2-PPA. **c**, Hammett plot for the oxidation of *para*-Y-Ph-CHO [Y = OMe, Me, H, Cl] by **1** in CH_3CN at 5 ^oC.

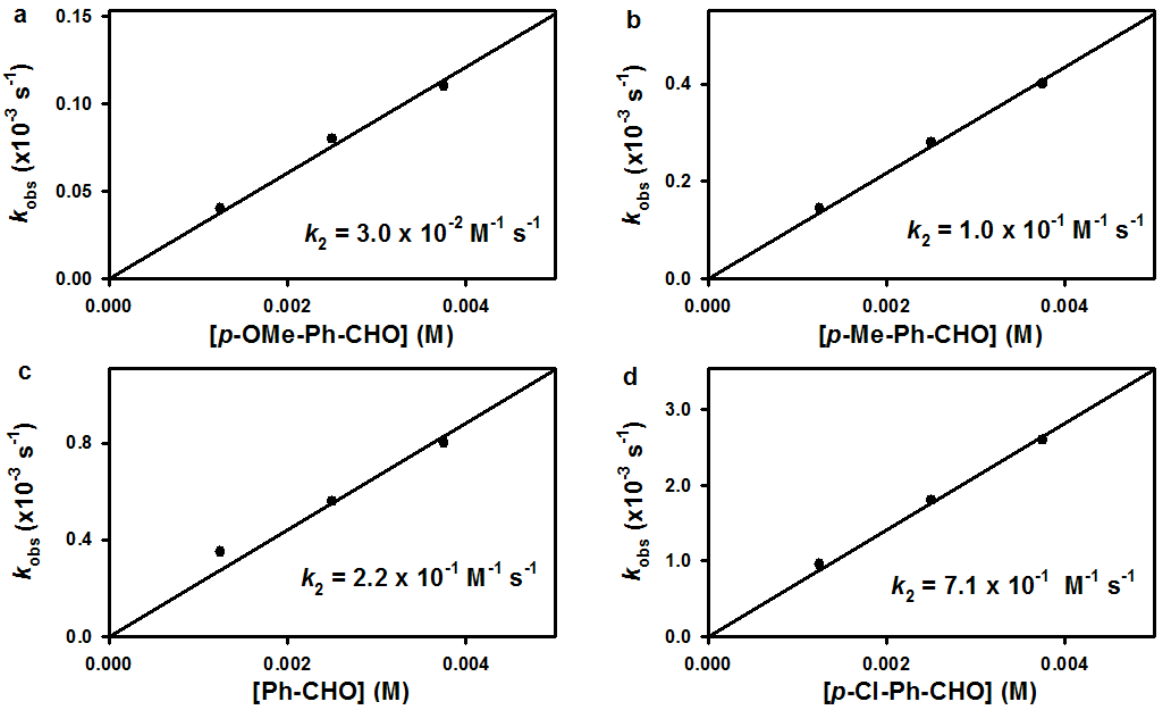

Supplementary Figure 7. Plot of pseudo-first-order rate constants (k_{obs}) against the concentration of *para*-Y-Ph-CHO [Y = OMe (**a**), Me (**b**), H (**c**), Cl (**d**)] in the deformylation of aldehyde by **1** in CH_3CN at 5 ^{o}C.

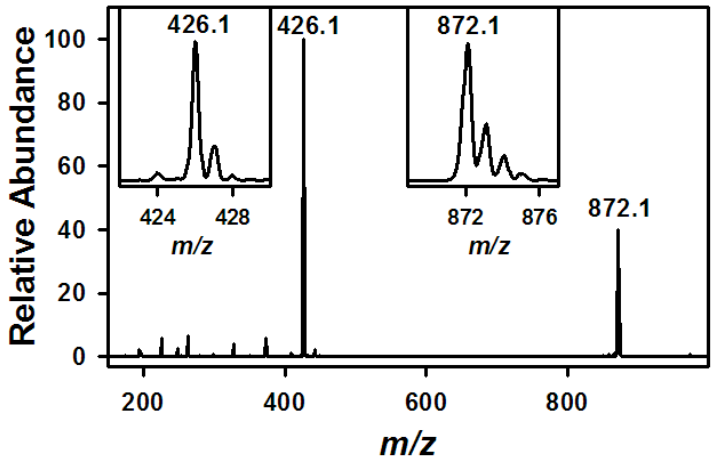

Supplementary Figure 8. Negative mode ESI MS spectrum taken after completion of the O_2-transfer reaction between **1** and $[Mn^{III}(TAML)]^-$ in CH_3CN/DMF (1:4) at –20 ^oC. The peaks at *m/z* 426.1 and 872.1 correspond to $[Fe(TAML)]^-$ (calculated *m/z* of 426.1) and $[K(2.2.2\text{-cryptand})Mn(TAML)(O_2)]^-$ (**2**, calculated *m/z* of 876.3), respectively. Insets show the observed isotope distribution patterns for $[Fe(TAML)]^-$ at *m/z* 426.1 (left panel) and **2** at *m/z* 872.1 (right panel).

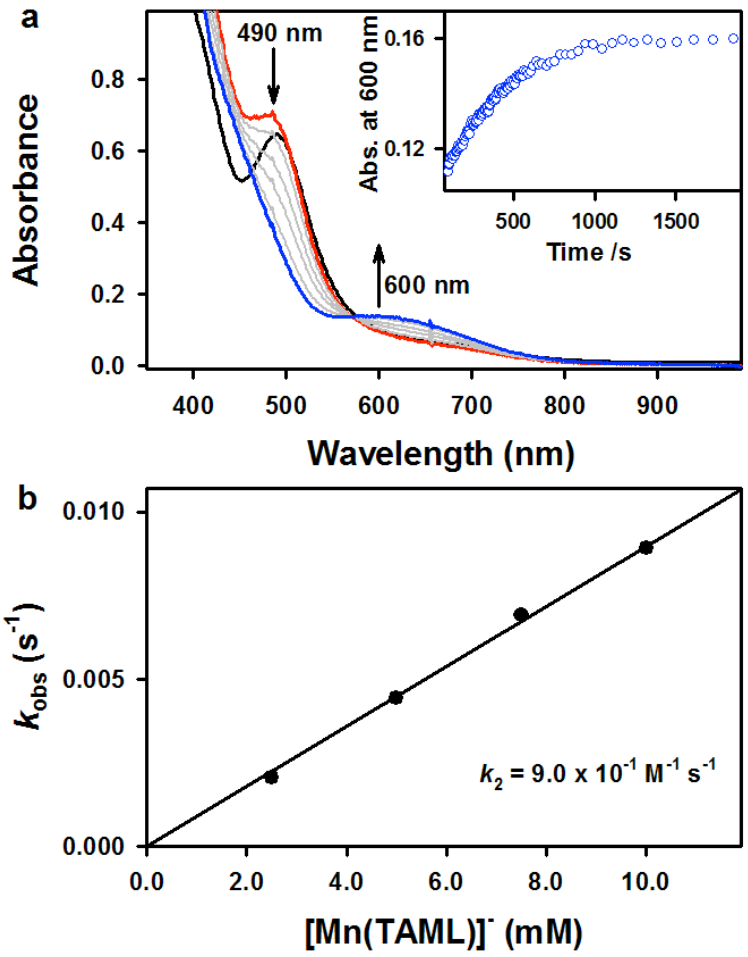

Supplementary Figure 9. **a**, UV-vis spectral changes showing the formation of **2** at 600 nm upon addition of $[Mn^{III}(TAML)]^-$ (2.5 mM) to a solution of **1** (0.25 mM) in DMF at –20 ^oC. An isosbestic point was observed at 573 nm. Inset shows the time traces at 600 nm (blue circle) for the formation of **2**. **b**, Plots of pseudo-first-order rate constants (k_{obs}) against concentration of **3** (2.5 – 10 mM) to determine the second-order rate constant (k_2) in DMF at –20 ^oC.

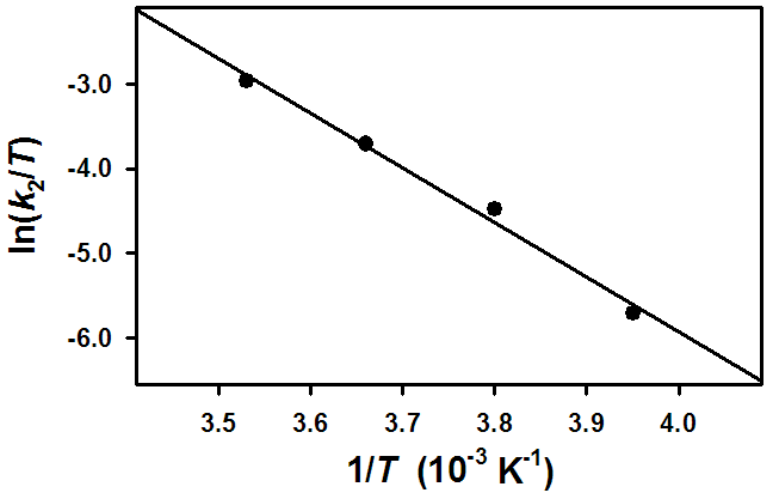

Supplementary Figure 10. Eyring plot of $\ln(k_2/T)$ against $1/T$ in the reaction of **1** with $[Mn^{III}(TAML)]^-$ in DMF between –20 and 10 °C. The activation parameters were determined to be $\Delta H^{\ddagger} = 54$ kJ mol^{-1} and $\Delta S^{\ddagger} = -40$ J mol^{-1} K^{-1}.

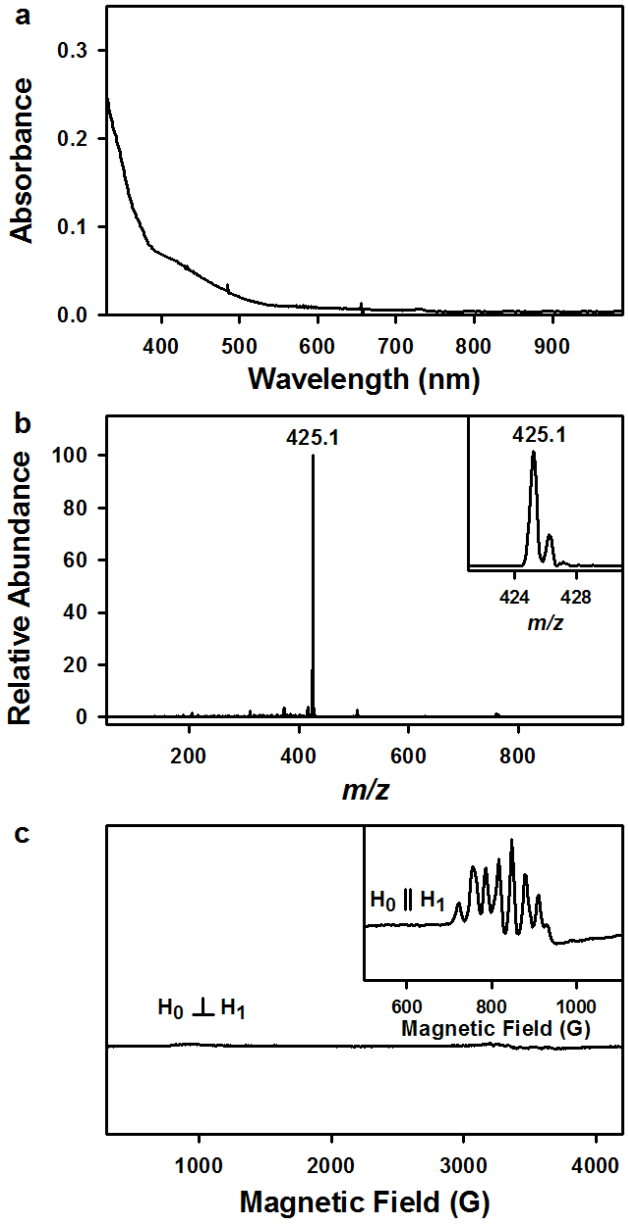

Supplementary Figure 11. **a**, UV-vis spectrum of $Li(CH_3OH)_2[Mn^{III}(TAML)(CH_3OH)]$ (0.25 mM) in CH_3OH. **b**, A negative mode ESI MS spectrum of $[Mn^{III}(TAML)]^-$ (0.25 mM) in CH_3OH. The peak at *m/z* = 425.1 corresponds to $[Mn(TAML)]^-$ (calculated *m/z* of 425.1). Inset shows the observed isotope distribution pattern for $[Mn(TAML)]^-$. **c**, X-band EPR spectrum of $[Mn^{III}(TAML)]^-$ (1.0 mM) recorded in CH_3OH at 4.3 K. Inset shows X-band parallel-mode EPR spectrum of $[Mn^{III}(TAML)]^-$ (1.0 mM) with six-line hyperfine pattern centered at $g = 8.1$ with splitting of $a = 30$ G. Spectral conditions: microwave power = 1.0 mW, frequency = 9.647 GHz, receive gain = 1.0×10^4, modulation amplitude = 10 G, and modulation frequency = 100 kHz.

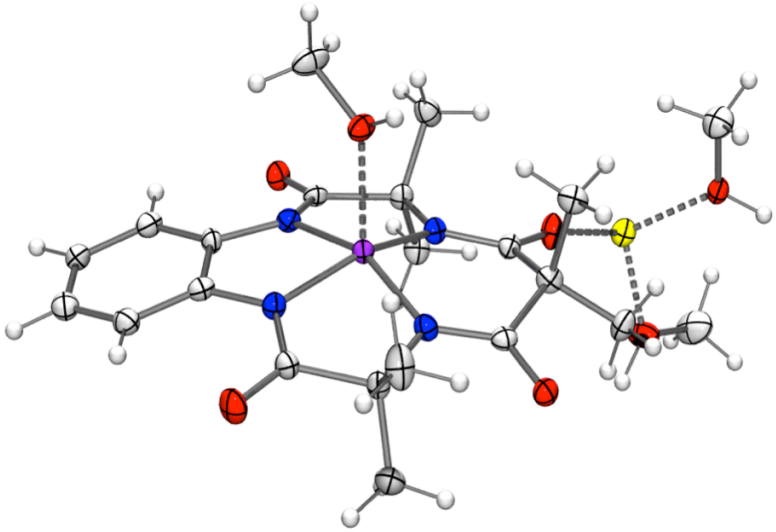

Supplementary Figure 12. X-ray crystal structure of $[Li(CH_3OH)_2][Mn^{III}(TAML)(CH_3OH)]$, with thermal ellipsoids drawn at the 30% probability level, produced using ORTEP software. White, H; Gray, C; blue, N; red, O; cyan, Mn; yellow, Li. Selected bond distances (Å) and angles (deg) for $[Mn^{III}(TAML)]^-$ are summarized in Table 3.

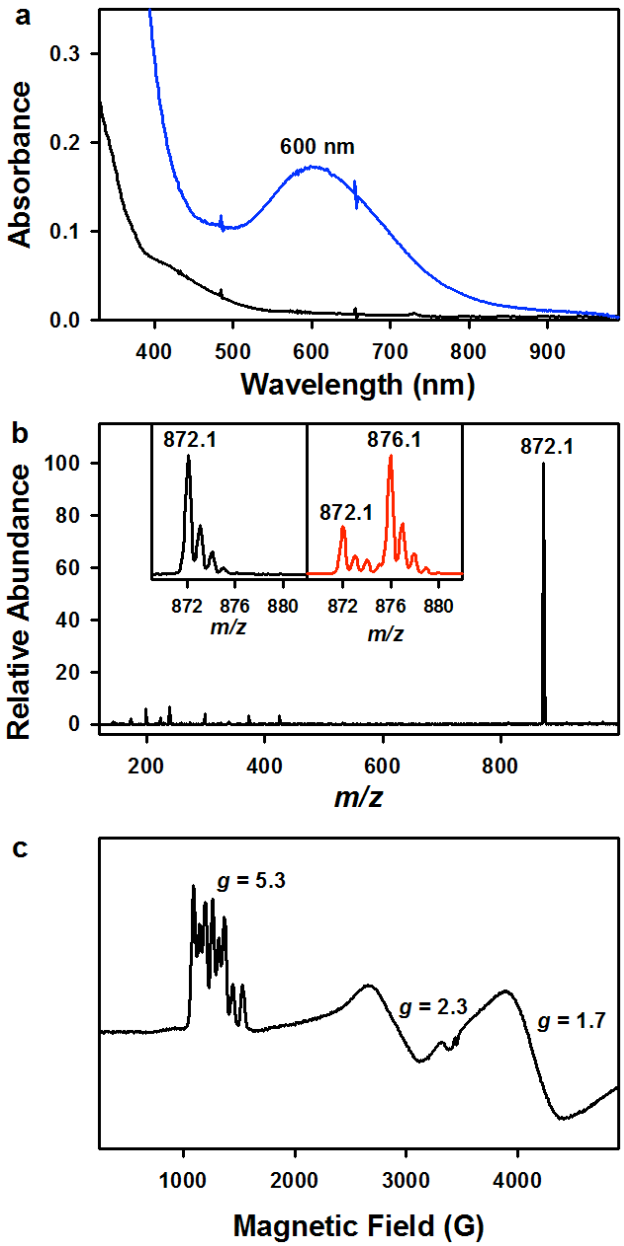

Supplementary Figure 13. **a**, UV-vis spectrum of $[Mn^{IV}(TAML)(O_2)]^{2-}$ (**2**, 0.25 mM). **b**, Negative mode ESI MS spectrum of **2** (0.25 mM) in CH_3CN. Insets show the observed isotope distribution patterns of $[K(2.2.2\text{-cryptand})Mn(TAML)(^{16}O_2)]^-$ (**2-$^{16}O_2$**, left panel) at *m/z* of 872.1 (calculated *m/z* of 872.3) and $[K(2.2.2\text{-cryptand})Mn(TAML)(^{18}O_2)]^-$ (**2-$^{18}O_2$**, right panel) at *m/z* of 876.1 (calculated *m/z* of 876.3). **c**, X-band EPR spectrum of **2** (1.0 mM) recorded in CH_3CN at 4.3 K. Spectral conditions: microwave power = 1.0 mW, frequency = 9.647 GHz, receive gain = 1.0×10^4, modulation amplitude = 10 G, and modulation frequency = 100 kHz.

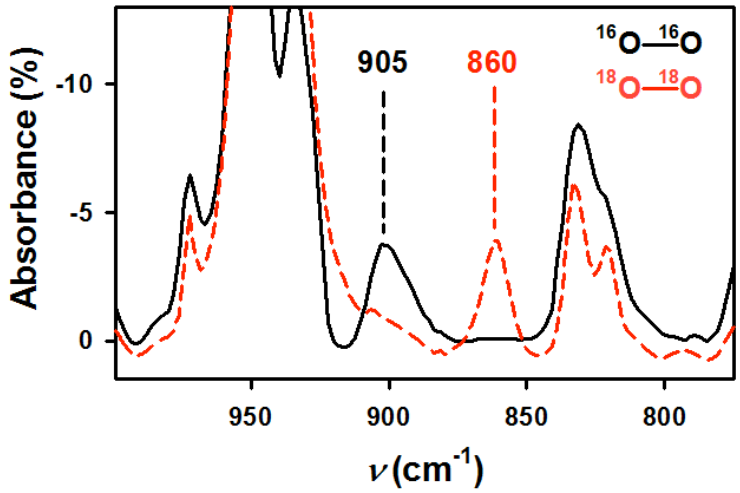

Supplementary Figure 14. FT-IR spectra of **2-$^{16}O_2$** (black line) and **2-$^{18}O_2$** (red line).

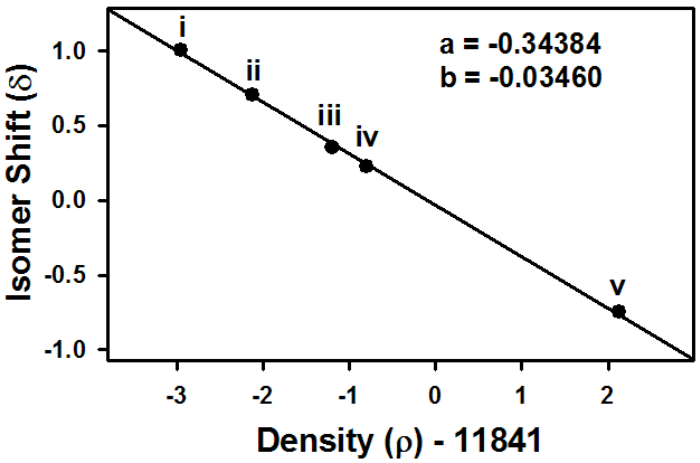

Supplementary Figure 15. Calibration of calculated density at the nucleus to known isomer shift values for five complexes (in order of decreasing isomer shift: $Fe(SCH_3)_4^-$ (i), $FeCl_4^-$ (ii), $Fe(SCH_3)_4)^{2-}$ (iii), $FeCl_4^{2-}$ (iv), and ferrate (v)) using the BP86 functional mixed with 25%HF exchange, the CP(PPP) basis set on Fe, and TZVP on the other atoms. The best-fit equation is $\delta = a(\rho - 11841) + b$.

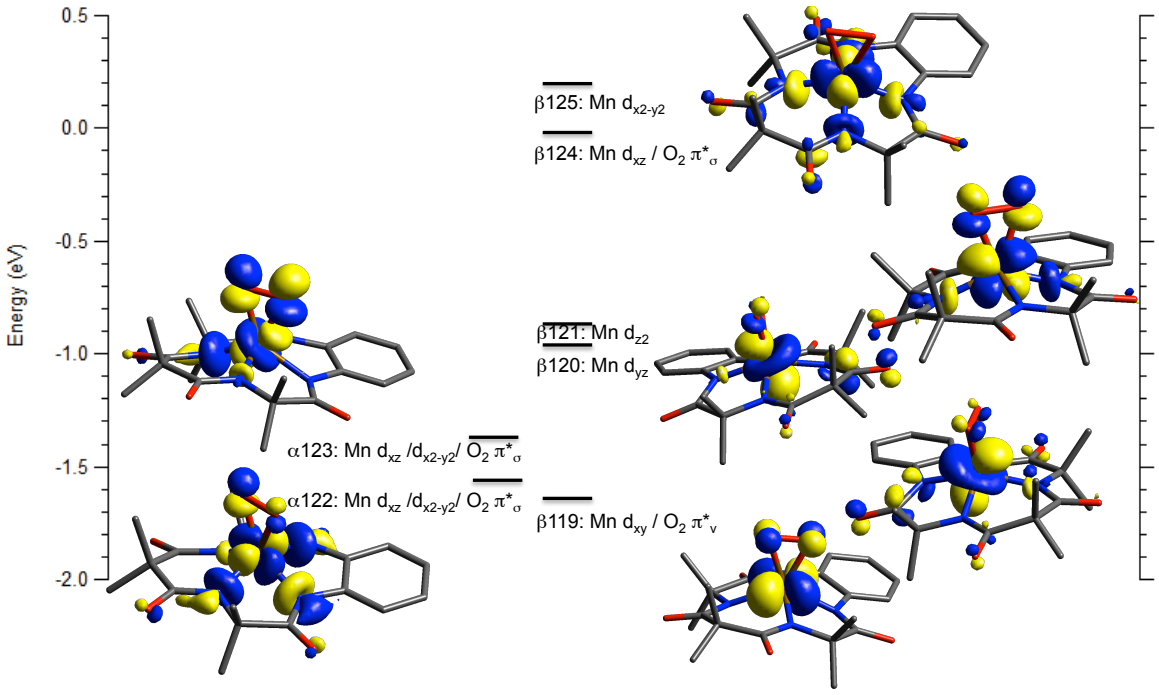

Supplementary Figure 16. DFT calculations on **2** showing unoccupied MOs for **2** with significant Mn or O_2 π* character.

Supplementary Table 1. Selected bond distances (Å) and angles (°) for **1**.

Crystallographically independent moiety 1			
Fe1-O1	1.932(2)	Fe1-N3	1.926(2)
Fe1-O2	1.902(2)	Fe1-N4	1.909(2)
Fe1-N1	1.909(2)	O1-O2	1.323(3)
Fe1-N2	1.914(2)		
O1-Fe1-O2	40.37(9)	O2-O1-Fe1	68.58(14)
O1-O2-Fe1	71.05(14)		

Crystallographically independent moiety 2[a]			
Fe2-O7	1.912(5)	Fe2-N5	1.905(2)
Fe2-O8	1.920(4)	Fe2-N6	1.921(2)
Fe2-O7’	1.942(8)	Fe2-N7	1.921(2)
Fe2-O8’	1.957(10)	Fe2-N8	1.898(2)
O7-O8	1.306(7)	O7’-O8’	1.315(12)
O7-Fe2-O8	39.9(2)	O7’-Fe2-O8’	39.4(4)
O7-O8-Fe2	69.8(3)	O7’-O8’-Fe2	69.7(6)
O8-O7-Fe2	70.4(3)	O8’-O7’-Fe2	70.9(6)

[a] The second independent moiety of **1** has the positional disorder of superoxo moiety (O7-O8 and O7’-O8’).

Supplementary Table 2. Selected bond distances (Å) and angles (°) for **2**.

Crystallographically independent moiety 1			
Mn1-O1	1.8697(15)	Mn1-N3	1.9702(18)
Mn1-O2	1.8823(15)	Mn1-N4	1.9519(18)
Mn1-N1	1.9553(17)	O1-O2	1.415(2)
Mn1-N2	1.9437(17)		
O1- Mn1-O2	44.30(7)	O2-O1- Mn1	68.32(9)
O1-O2- Mn1	67.38(9)		

Crystallographically independent moiety 2[a]			
Mn2-O7	1.876(2)	Mn2-N5	1.9487(18)
Mn2-O8	1.8793(19)	Mn2-N6	1.9521(19)
Mn2-O7’	1.903(10)	Mn2-N7	1.9576(18)
Mn2-O8’	1.849(10)	Mn2-N8	1.9456(18)
O7-O8	1.412(3)	O7’-O8’	1.403(13)
O7- Mn2-O8	44.17(10)	O7’- Mn2-O8’	43.9(4)
O7-O8- Mn2	67.79(12)	O7’-O8’-Mn2	70.1(6)
O8-O7- Mn2	68.05(12)	O8’-O7’- Mn2	66.0(6)

[a] The second independent moiety of **2** has the positional disorder of superoxo moiety (O7-O8 and O7’-O8’).

Supplementary Table 3. Selected bond distances (Å) and angles (°) for $[Li(CH_3OH)_2][Mn^{III}(TAML)(CH_3OH)]$.

	$[Li(CH_3OH)_2][Mn^{III}(TAML)(CH_3OH)]$
Bond Distances	
Mn1-N1	1.910(3)
Mn1-N2	1.906(3)
Mn1-N3	1.923(3)
Mn1-N4	1.908(3)
Mn1-O5	2.239(2)
Bond Angles (°)	
N1-Mn1-N2	83.11(13)
N1-Mn1-N3	157.13(12)
N1-Mn1-N4	84.57(12)
N1-Mn1-O5	95.82(10)
N2-Mn1-N3	84.69(12)
N2-Mn1-N4	155.66(12)
N2-Mn1-O5	99.47(11)
N3-Mn1-N4	99.16(11)
N3-Mn1-O5	105.24(10)

Supplementary Table 4. Comparison of geometry around the Fe center for **1** from crystallography and DFT using various functionals and the TZVP basis set. The BP86 functional mixed with 25% HFX gives the best overall agreement with the crystallography.

	Fe-O bond (ave, in Å)	O-O bond (Å)	Fe-N bond (ave, in Å)
Crystal	1.92	1.32	1.91
BP86 + 10% HFX	1.99	1.35	1.92
BP86	1.92 (1.84, 2.00)	1.43	1.93
TPSSh	1.89 (1.86, 1.91)	1.42	1.92
B3LYP	1.94	1.39	1.94
M06	2.06	1.34	1.92

Supplementary Table 5. Comparison of geometry around the Mn center for **2** from crystallography and DFT using various functionals and the TZVP basis set. B3LYP gives the best agreement with crystallography than BP86.

	Mn-O bond (ave, in Å)	O-O bond (Å)	Mn-N bond (ave, in Å)
Crystal	1.88	1.42	1.95
B3LYP	1.89	1.42	1.94
BP86	1.89	1.43	1.97
TPSSh	1.87	1.43	1.96
M06	1.93	1.38	1.96

Supplementary Table 6. Calculated ionization energies (in eV) for M(III)-TAML-X, going to M(IV)-TAML-X and a final spin state of $S = 1$ for Fe and $S = 3/2$ for Mn. All energies correspond to geometry-optimized structures.

Starting oxidation and spin state	X = Cl^-	X = O_2^{2-}
Fe(III) ($S = 3/2$)	4.82	2.91
Mn(III) ($S = 2$)	4.82	2.90
Mn(III) ($S = 1$)	3.58	2.49

Supplementary Methods

Materials. All chemicals obtained from Aldrich Chemical Co. were the best available purity and used without further purification unless otherwise indicated. Solvents were dried according to published procedures and distilled under Ar prior to use[1]. $K^{18}O_2$ (90% ^{18}O-enriched) was purchased from ICON Services Inc. (Summit, NJ, USA). $Na[Fe^{III}(TAML)]$ and TAML-H_4 (TAML = tetraamido marcrocyclic ligand, 3,3,6,6,9,9-hexametyl-2,5,7,10-tetraoxo-3,5,6,7,9,10-hexahydro-2*H*-benzo[*e*][1,4,7,10]tetraazacyclo-tridecine-1,4,8,11-tetraide) were purchased from GreenOx Catalyst, Inc. (Pittsburgh, PA, USA). The commercial complex was recrystallized from an isopropanol/H_2O mixture for further use[2]. ^{57}Fe-enriched complex **1** was prepared according to the literature method[2]. $Li(CH_3OH)_2[Mn^{III}(TAML)(CH_3OH)]$ was synthesized by deprotonating TAML-H_4 (450 mg, 1.2 mmol) ligand with lithium *bis*(trimethylsilyl)amide (6.3 mL of 1.0 M THF solution, 6.3 mmol), followed by addition of $Mn(acac)_3$ (550 mg, 1.6 mmol) under Ar in dry and deoxygenated tetrahydrofuran (THF) (40 mL) at 25 ^oC[3,4]. The reaction mixture was stirred (5 hours) and then the solvent was removed on a rotary evaporator, giving a reddish orange solid. The solid was dissolved in water and filtered, and then the filtrate was evaporated to dryness under reduced pressure, leaving reddish orange solid in ~70 % yield (440 mg). Negative ESI MS in CH_3OH (see Supplementary Fig. 11); *m/z* 425.1 for $[Mn(TAML)]^-$. Reddish orange crystals suitable for X-ray analysis were successfully grown by storing a solution of $[Mn(TAML)]^-$ in CH_3OH/diethyl ether (1:10) at 25 °C. Anal. Calcd for $C_{22}H_{34}LiMnN_4O_7$: C, 50.01; H, 6.49; N, 10.60. Found C, 49.80; H, 6.71; N, 10.45. The dimeric product of 2,4-di-*tert*-butylphenol, 2,2'-dihydroxy-3,3',5,5'-tetra-*tert*-butyldiphenol, was prepared by published procedures[5].

Instrumentations. UV-vis spectra were recorded on a Hewlett Packard 8453 diode array spectrophotometer equipped with a UNISOKU Scientific Instruments for low-temperature experiments or with a circulating water bath. Electrospray ionization mass (ESI MS) spectra were collected on a Thermo Finnigan (San Jose, CA, USA) LCQ^{TM} Advantage MAX quadrupole ion trap instrument by infusing samples directly into the source at 20 μL/min using a syringe pump. The spray voltage was set at 3.7 kV and the capillary temperature at 80 °C. X-band EPR spectra were recorded at 4.3 K using X-band Bruker EMX-plus spectrometer equipped with a dual mode cavity (ER 4116DM). Low temperature was achieved and controlled with an Oxford Instruments ESR900 liquid He quartz cryostat with an Oxford Instruments ITC503 temperature and gas flow controller. The experimental parameters for EPR were as follows: Microwave frequency = 9.647 GHz, microwave power = 1.0 mW, modulation amplitude = 10 G, gain = 1.0×10^4, modulation frequency = 100 kHz, time constant = 40.96 ms, and conversion time = 81.00 ms. ^{1}H NMR spectra were measured with Bruker DPX-400 spectrometer. Infrared spectra were recorded on a REMSPEC Reaction View FT-IR spectrometer equipped with a Fiber Optic Immersion Probe or Varian FT-IR Scimitar Series 800 with KBr solid. Product analysis was performed using high performance liquid chromatography (HPLC, Waters 515) and gas chromatography (GC, Agilent Technology 6890N) equipped with a FID detector.

Generation of $[Fe^{III}(TAML)(O_2)]^{2-}$ (1) and $[Mn^{IV}(TAML)(O_2)]^{2-}$ (2). 1 was generated by adding excess solid potassium superoxide (KO_2) (10 mg, 141 μmol) to a solution of $Na[Fe^{III}(TAML)]$ (10 mg, 15 μmol) in the presence of six equivalents of 4,7,13,16,21,24-hexaoxa-1,10-diazabicyclo[8.8.8]hexacosane (2.2.2-cryptand) (33 mg, 88 μmol) in CH_3CN (2.0 mL) at 5 ^oC. Immediate colour change from reddish yellow to deep red was observed. **1** then was treated with Et_2O (20 mL) and stored to yield deep red

crystals in CH_3CN at –20 °C. $^{18}O_2$-incorporated **1**, $[Fe^{III}(TAML)(^{18}O_2)]^{2-}$ (**1-$^{18}O_2$**), was obtained by adding excess ^{18}O-labeled KO_2 (2.8 mg, 40 μmol) to the solution of $Na[Fe^{III}(TAML)]$ (4.0 mM) in the presence of six equivalents of 2.2.2-cryptand (9.3 mg, 25 μmol) in CH_3CN (2.0 mL) at –20 °C. Negative mode ESI MS in CH_3CN (Supplementary Fig. 3): *m/z* 873.1 for $[K(2.2.2\text{-cryptand})Fe(TAML)(^{16}O_2)]^-$ and *m/z* 877.1 for $[K(2.2.2\text{-cryptand})Fe(TAML)(^{18}O_2)]^-$. Crystals suitable for X-ray analysis were successfully grown by storing a solution of **1** in CH_3CN/diethyl ether (1:5) at –20 °C, and the yield of crystals was ~70 %. Infrared spectra of **1-$^{16}O_2$** and **1-$^{18}O_2$** (4.0 mM) were recorded in CH_3CN (2.0 mL) at –40 °C.

The spin state of **1** was determined using the modified ^1H NMR method of Evans at room temperature[6-8]. A WILMAD® coaxial insert (sealed capillary) tube containing the blank acetonitrile-d_3 solvent (with 1.0% TMS) was inserted into the normal NMR tubes containing the complexes (4.0 mM) dissolved in acetonitrile-d_3 (with 0.1% TMS). The chemical shift of the TMS peak in the presence of the paramagnetic metal complexes was compared to that of the TMS peak in the outer NMR tube. The magnetic moment was calculated using the following equation,

$$\mu = 0.0618(\Delta vT / 2fM)^{1/2}$$

where f is the oscillator frequency (MHz) of the superconducting spectrometer, T is the absolute temperature, M is the molar concentration of the metal ion, and v is the difference in frequency (Hz) between the two reference signals[8]. ^1H NMR Evans method allowed us to determine magnetic moment of 3.26 μ_B in CH_3CN at -20 °C

2 was generated by introducing excess amount of solid KO_2 (10 mg, 141 μmol) to a solution of $Li[Mn^{III}(TAML)]$ (10 mg, 14.7 μmol) in the presence of six equivalents of 2.2.2-cryptand (33 mg, 88.2 μmol) in CH_3CN (2.0 mL) at 25 °C. Slow color change from

orange to blue (~3 h) was observed. **2** was thermally stable at 25 ^{o}C. **2** was then treated with Et_2O (20 mL) and stored to yield blue crystals in CH_3CN at –20 ^{o}C. $^{18}O_2$-incorporated **2** (4.0 mM), $[Mn^{IV}(TAML)(^{18}O_2)]^{2-}$ (**2-^{18}O$_2$**), was obtained by adding excess ^{18}O-labeled KO_2 (2.8 mg, 40 μmol) in the presence of six equivalents of 2.2.2-cryptand (9.3 mg, 25 μmol) in CH_3CN (2.0 mL) at 5 ^{o}C. Negative mode ESI MS in CH_3CN (Supplementary Fig. 13): *m/z* 872.1 for $[K(2.2.2\text{-cryptand})Mn(TAML)(^{16}O_2)]^{-}$ and *m/z* 876.1 for $[K(2.2.2\text{-cryptand})Mn(TAML)(^{18}O_2)]^{-}$. Crystals suitable for X-ray analysis were successfully grown by storing a solution of **2** in CH_3CN/diethyl ether (1:5) at –20 °C, and the yield of crystals was ~70 %. Infrared spectra (KBr) of **2-^{16}O$_2$** and **2-^{18}O$_2$** were obtained at room temperature.

X-ray Crystallography. Single crystals of $[K(2.2.2\text{-cryptand})(CH_3CN)][K(2.2.2\text{-cryptand})]_3[Fe^{III}(TAML)(O_2)]_2$, $[K(2.2.2\text{-cryptand})(CH_3CN)][K(2.2.2\text{-cryptand})]_3[Mn^{IV}(TAML)(O_2)]_2$, and $[Li(CH_3OH)_2][Mn^{III}(TAML)(CH_3OH)]$ were picked from solutions by a nylon loop (Hampton Research Co.) on a hand made copper plate mounted inside a liquid N_2 Dewar vessel at *ca*. –20 °C and mounted on a goniometer head in a N_2 cryostream. Data collections were carried out either at 100(2) or 170(2) K (only for $[Li(CH_3OH)_2][Mn^{III}(TAML)(CH_3OH)]$) on a Bruker SMART AXS diffractometer equipped with graphite-monochromated Mo *K*α radiation (λ = 0.71073 Å). The CCD data were integrated and scaled using the Bruker-SAINT software package. All structures were solved with the program SHELXS-97 (Sheldrick, 2008) and were refined on F^2 with SHELXL-97 (Sheldrick, 2008). The H atoms were placed at calculated positions using the instructions AFIX 23, AFIX 43 or AFIX 137 with isotropic displacement parameters having values 1.2 or 1.5 times *U*eq of the attached C atoms[9].

Crystal data for $[K(2.2.2\text{-cryptand})(CH_3CN)][K(2.2.2\text{-cryptand})]_3[Fe^{III}(TAML)(O_2)]_2$: '$2(C_{19}H_{22}FeN_4O_6)$, $C_{20}H_{39}KN_3O_6$, $3(C_{18}H_{36}KN_2O_6)$', Fw = 2619.92, red block, 0.20 × 0.20

× 0.20 mm^3, monoclinic, $P2_1/n$ (no. 14), a = 23.3521(4), b = 25.7445(4), c = 24.3380(4) Å, β = 113.8390(10)°, V = 13383.4(4) $Å^3$, Z = 4, D_x = 1.300 g cm^{-3}, μ = 0.421 mm^{-1}, abs. corr. range: 0.9205 – 0.9205. 225503 Reflections were measured up to a resolution of (sin $\theta/\lambda)_{max}$ = 0.65 $Å^{-1}$. 30730 Reflections were unique (R_{int} = 0.0748), of which 17617 were observed [$I > 2\sigma(I)$]. 1835 Parameters were refined using 906 restraints. Data-to-parameter ratio = 16.7. $R1/wR2$ [$I > 2\sigma(I)$]: 0.0593/0.1316. $R1/wR2$ [all refl.]: 0.1160/0.1479. S = 1.047. Residual electron density found between −0.75 and 1.58 e $Å^{-3}$.

Crystal data for $[K(2.2.2\text{-cryptand})(CH_3CN)][K(2.2.2\text{-cryptand})]_3[Mn^{IV}(TAML)(O_2)]_2$: '$2(C_{19}H_{22}MnN_4O_6)$, $C_{20}H_{39}KN_3O_6$, $3(C_{18}H_{36}KN_2O_6)$', Fw = 2618.10, clear dark blue block, 0.20 × 0.10 × 0.10 mm^3, monoclinic, $P2_1/n$ (no. 14), a = 23.2548(6), b = 25.7982(6), c = 24.3509(6) Å, β = 113.6490(10)°, V = 13382.0(6) $Å^3$, Z = 4, D_x = 1.299 g cm^{-3}, μ = 0.393 mm^{-1}, abs. corr. range: 0.87 – 0.96. 227058 Reflections were measured up to a resolution of (sin $\theta/\lambda)_{max}$ = 0.65 $Å^{-1}$. 30741 Reflections were unique (R_{int} = 0.0731), of which 19752 were observed [$I > 2\sigma(I)$]. 1835 Parameters were refined using 912 restraints. Data-to-parameter ratio = 16.7. $R1/wR2$ [$I > 2\sigma(I)$]: 0.0506/0.1143. $R1/wR2$ [all refl.]: 0.0910/0.1262. S = 1.062. Residual electron density found between −0.85 and 0.50 e $Å^{-3}$.

The structures of **1** and **2** are isomorphous. In both structures, the $[K(2.2.2\text{-cryptand})(CH_3CN)]^+$ cation (containing the metal K3) is found to be wholly disordered over two orientations, and the occupancy factors of the major components of the disorder refine to 0.557(5) for **1** and 0.516(5) for **2**. The O_2 molecule O7-O8 (coordinated to Fe2) is also found to be disordered over two orientations. The two orientations of O_2 may be related by a rotation of about 90° along the direction perpendicular to the base of the square pyramidal geometry. The occupancy factors of the major components of the disorder refine to 0.650(7) for **1** and 0.824(4) for **2**.

In both structures, the crystal lattice also contains some amounts of disordered solvent molecules (most likely to be one diethyl ether lattice molecule per asymmetric unit whose occupancy factors are possibly lower than 1). The contribution of the lattice solvent molecule has been taken out using the program SQUEEZE (Spek, 2003) for the final refinement[10]. All details of the SQUEEZE refinement are provided in the CIF files.

Crystal data for $[Li(CH_3OH)_2][Mn^{III}(TAML)(CH_3OH)]$: $C_{22}H_{34}LiMnN_4O_7$, Fw = 528.41, pale yellow needle, 0.10 × 0.05 × 0.05 mm^3, *Orthorhombic*, *Pna2₁*, a = 11.5326(16), b = 22.552(3), c = 9.7122(13) Å, V = 2525.9(6) $Å^3$, Z = 4, D_x = 1.390 g/cm^3, μ = 0.570 mm^{-1}, abs. corr. range: 0.9452 – 0.9720. 36897 Reflections were measured up to a resolution of $(\sin \theta/\lambda)_{max}$ = 0.62 $Å^{-1}$. 4940 Reflections were unique (R_{int} = 0.0913), of which 4085 were observed [$I > 2\sigma(I)$]. 325 Parameters were refined using 1 restraint. Data-to-parameter ratio = 15.2. $R1/wR2$ [$I > 2\sigma(I)$]: 0.0401/0.1030. $R1/wR2$ [all refl.]: 0.0550/0.1169. S = 0.779. Residual electron density found between −0.54 and 0.24 e $Å^{-3}$.

Supplementary Table 1 lists the selected bond distances and angles. CCDC-1001933 for $[K(2.2.2\text{-cryptand})(CH_3CN)][K(2.2.2\text{-cryptand})]_3[Fe^{III}(TAML)(O_2)]_2$ contains the supplementary crystallographic data for this paper. Supplementary Table 2 lists the selected bond distances and angles. CCDC-1001934 for $[K(2.2.2\text{-cryptand})(CH_3CN)][K(2.2.2\text{-cryptand})]_3[Mn^{IV}(TAML)(O_2)]_2$ contains the supplementary crystallographic data for this paper. Supplementary Table 3 lists the selected bond distances and angles. CCDC-1001935 for $[Li(CH_3OH)_2][Mn^{III}(TAML)(CH_3OH)]$ contains the supplementary crystallographic data for this paper. These data can be obtained free of charge via www.ccdc.cam.ac.uk/data_request/cif (or from the Cambridge Crystallographic Data Centre, 12, Union Road, Cambridge CB2 1EZ, UK; fax: (+44) 1223-336-033; or deposit@ccdc.cam.ac.uk).

Mössbauer Analysis. Mössbauer spectra were recorded at 4.2 K in a Janis model SVT-400T cryostat. Spectral simulations were carried out using the WMOSS software package (WEB research, Minneapolis, MN). All isomer shifts are quoted relative to Fe foil at 298K.

Density Functional Theory. Density functional theory (DFT) calculations were performed with the Gaussian 09 software package[11], using both the unrestricted B3LYP functional[12,13] and the unrestricted BP86 functional[14] without and with 25% Hartree-Fock exchange, the TPSSh functional[15], and the M06 functional[16]. The Pople triple-ς basis set 6-311G[17] and the TZVP basis set[18] were both used, 6-311G for Mössbauer calibration and TZVP for geometry optimizations and for electronic structure elucidation. Solvent effects were included by applying the polarized continuum model (PCM)[19] using the dielectric constant of acetonitrile, $\varepsilon = 35.67$, the solvent used in the experiments. All optimized structures were found to be stable, with no imaginary frequency. In order to obtain calculated isomer shift values, the optimized structures were used as the input in ORCA[20] and single-point calculations were carried out using the same functional. This gave the density at the nucleus ρ and the quadrupole splitting ΔE_Q. For geometry optimizations using the 6-311G basis set, the same basis set was used in the ORCA calculations. For the geometry optimized structures in Gaussian using the TZVP basis set, Mössbauer parameters were calculated using the ORCA program with the CP(PPP) basis set[21] on Fe and the TZVP basis set on the other atoms, in addition to the auxiliary basis sets TZV/J (Fe) and SV/J (other atoms) from the Turbomole library[22,23]. Molecular orbital contours were generated using the program LUMO, and Mulliken populations of the orbitals were calculated using QMForge[24,25].

Kinetic Measurements. All reactions were run in a 1-cm UV cuvette by monitoring

UV-vis spectral changes of reaction solutions, using isolated complex **1** directly in all reactions. Pseudo-first order rates for the O-H bond activation reactions between **1** and 2,4-di-*tert*-butylphenol and *para*-Y-2,6-di-*tert*-butylphenol (*p*-Y-2,6-*t*-Bu_2-C_6H_2OH; Y = OMe, Me, H, CN) and for the aldehyde deformylation reactions between **1** and 2-phenylpropionaldehyde (2-PPA) and *para*-substituted benzaldehyde (*para*-Y-Ph-CHO; Y = OMe, Me, H, Cl) were determined by fitting the absorbance changes at 490 nm for **1** in CH_3CN at 5 °C. The kinetic studies for the O_2-transfer from **1** to $[Mn^{III}(TAML)]^-$ were performed in dimethylformamide (DMF) at given temperatures. Rate constants of O_2-transfer were determined by fitting the decay of the absorption band corresponding to **1** (0.25 mM) at 490 nm or the formation of the absorption band corresponding to **2** at 600 nm. All kinetic measurements were carried out under pseudo-first-order conditions, where the concentration of **3** (2.5 – 10 mM) was maintained to be more than 10-folds excess of **1**. The O_2-transfer from **1** to $[Mn^{III}(TAML)]^-$ was further confirmed by taking ESI MS of the reaction mixture. Mixing equimolar amounts of **1** and $[Mn^{III}(TAML)]^-$ resulted in a disappearance in the mass peak corresponding to **1** (*m/z* 873.1 for [K(2.2.2-cryptand)Fe(TAML)$(O_2)]^-$) with a concomitant appearance in the peaks corresponding to **2** (*m/z* 872.1 for [K(2.2.2-cryptand)Mn(TAML)$(O_2)]^-$) and $[Fe(TAML)]^-$ (*m/z* 426.1) (Supplementary Fig. 8).

Temperature-dependent kinetic experiments were performed with **1** (0.25 mM) in DMF between 10 and –20 °C in order to determine activation parameters. Pseudo-first-order fitting of the kinetic data allowed us to determine k_{obs} values for the decay of **1**. Reactions were run at least triplicate, and the data reported represent the average of these reactions.

Product Analysis. Products formed in the reaction of **1** and 2,4-di-*tert*-butylphenol

and 2-PPA were analyzed by GC and HPLC. Quantitative analyses were done by comparison against standard curves prepared with known authentic samples and using decane as an internal standard. In the oxidation of 2,4-di-*tert*-butylphenol by **1**, C-C coupled dimer product, 2,2'-dihydroxy-3,3',5,5'-tetra-*tert*-butylbiphenyl was produced with 75% yield[26]. In the reaction of **1** and 2-PPA, acetophenone was the major product with ~95% yield.

Supplementary References

1. Armarego, W. L. F. & Chai, C. L. L. *Purification of Laboratory Chemicals,* 6th ed.; Pergamon Press: Oxford, 2009.
2. Horwitz, C. P. & Ghosh, A. Carnegie Mellon University, PA, USA, 2006. To be found under http://www.chem.cmu.edu/groups/collins/patents/
3. Collins, T. J. & Gordon-Wylie, S. W. A manganese(V)-oxo complex. *J. Am. Chem. Soc.* **111**, 4511-4513 (1989).
4. Collins, T. J., Powell, R. D., Slebondnick, C. & Uffelman, E. S. A water-stable manganese(V)-oxo complex: definitive assignment of a $\nu_{Mn^{V}=O}$ infrared vibration. *J. Am. Chem. Soc.* **112**, 899-901 (1990).
5. van der Vlugt, J. I. *et al*. Sterically demanding diphosphonite ligands – synthesis and application in nickel-catalyzed isomerization of 2-methyl-3-butenenitrile. *Adv. Synth. Catal.* **346**, 993-1003 (2004).
6. Evans, D. F. The determination of the paramagnetic susceptibility of substances in solution by nuclear magnetic resonance. *J. Chem. Soc.* 2003-2005 (1959).
7. Lölinger, J. & Scheffold, R. Paramagnetic moment measurements by nmr. A micro technique. *J. Chem. Edu*. 646-647 (1972).

8. Evans, D. F. & Jakubovic, D. A. Water-soluble hexadentate Schiff-base ligands as sequestrating agents for iron(III) and gallium(III). *J. Chem. Soc. Dalton Trans.* 2927-2933 (1988).

9. Sheldrick, G. M. A short history of *SHELX*. *Acta Cryst.* **A64**, 112-122 (2008).

10. Spek, A. L. Structure validation in chemical crystallography. *Acta Cryst.* **D65**, 148-155 (2009).

11. Frisch, M. J. *et al*. Gaussian 09, Revision **C.01**, Gaussian, Inc., Wallingford CT, 2009.

12. Becke, A. D. Density−functional thermochemistry. III. The role of exact exchange. *J. Chem. Phys*. **98**, 5648-5652 (1993).

13. Lee, C. T., Yang, W. T. & Parr, R. G. Development of the Colle-Salvetti correlation-energy formula into a functional of the electron density. *Phys. Rev. B* **37**, 785-789 (1988).

14. Becke, A. D. Density-functional exchange-energy approximation with correct asymptotic behavior. *Phys. Rev. A: At. Mol. Opt. Phys.* **38**, 3098-3100 (1988).

15. Tao, J. M., Perdew, J. P., Staroverov, V. N. & Scuseria, G. E. Climbing the density functional ladder: nonempirical meta–generalized gradient approximation designed for molecules and solids. *Phys. Rev. Lett.* **91,** 146401 (2003).

16. Zhao, Y. & Truhlar, D. G. The M06 suite of density functionals for main group thermochemistry, thermochemical kinetics, noncovalent interactions, excited states, and transition elements: two new functionals and systematic testing of four M06-class functionals and 12 other functionals. *Theor. Chem. Acc.* **120,** 215-41(2008).

17. Krishnan, R., Binkley, J. S., Seeger, R. & Pople, J. A. Self-consistent molecular orbital methods. XX. A basis set for correlated wave functions. *J. Chem. Phys.* **72**,

650-654 (1980).

18. Schäfer, A., Huber, C. & Ahlrichs, R. Fully optimized contracted Gaussian basis sets of triple zeta valence quality for atoms Li to Kr. *J. Chem. Phys.* **100**, 5829-5835 (1994).

19. Cramer, C. J. & Truhlar, D. G. Implicit solvation models: equilibria, structure, spectra, and dynamics. *Chem. Rev.* **99**, 2161-2200 (1999).

20. Neese, F. ORCA – an ab initio, Density Functional and Semiempirical program package, Version 2.4. Max-Planck-Insitut für Bioanorganische Chemie, Mülheim and der Ruhr, 2004.

21. Neese, F. Prediction and interpretation of isomer shifts in ^{57}Fe mössbauer spectra by density functional theory. *Inorg. Chim. Acta* **337**, 181-192 (2002).

22. Eichkorn, K., Weigend, F., Treutler, O. & Ahlrichs, R. Auxiliary basis sets for main row atoms and transition metals and their use to approximate Coulomb potentials. *Theor. Chem.Acc.* **97**, 119-124 (1997).

23. Eichkorn, K., Treutler, O., Ohm, H., Häser, M. & Ahlrichs, R. Auxiliary basis sets to approximate Coulomb potentials. *Chem. Phys. Lett.* **240**, 283-289 (1995).

24. Kieber-Emmons, M. T. *LUMO*, Version 1.0.1.

25. Tenderholt, A. L. *QMForge*, Version 2.2, http://qmforge.sourceforge.net.

26. Lansky, D. E. & Goldberg, D. P. Hydrogen atom abstraction by a high-valent manganese(V)−oxo corrolazine. *Inorg. Chem.* **45**, 5119-5125 (2006).